

www.acsnano.org

Ion Transport in 2D Nanostructured π -Conjugated Thieno[3,2-b]thiophene-Based **Liquid Crystal**

Zhongyang Wang, Chaoqiuyu Wang, Yangyang Sun, Kai Wang, Joseph W. Strzalka, Shrayesh N. Patel,* Paul F. Nealey,* Christopher K. Ober,* and Fernando A. Escobedo*



Cite This: https://doi.org/10.1021/acsnano.2c07789



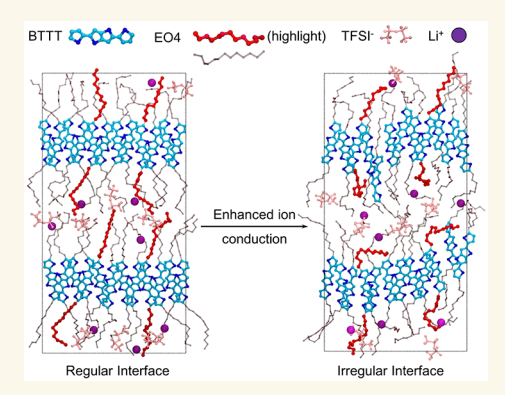
ACCESS I

Metrics & More

Article Recommendations

Supporting Information

ABSTRACT: Leveraging the self-assembling behavior of liquid crystals designed for controlling ion transport is of both fundamental and technological significance. Here, we have designed and prepared a liquid crystal that contains 2,5-bis(thien-2-yl)thieno[3,2-b]thiophene (BTTT) as mesogenic core and conjugated segment and symmetric tetra(ethylene oxide) (EO4) as polar side chains for ion-conducting regions. Driven by the crystallization of the BTTT cores, BTTT/dEO4 exhibits well-ordered smectic phases below 71.5 °C as confirmed by differential scanning calorimetry, polarized optical microscopy, temperature-dependent wide-angle X-ray scattering, and grazing incidence wideangle X-ray scattering (GIWAXS). We adopted a combination of experimental GIWAXS and molecular dynamics (MD) simulations to better understand the molecular packing of BTTT/dEO4 films, particularly when loaded with the ionconducting salt lithium bis(trifluoromethanesulfonyl)imide (LiTFSI). Ionic conduction of BTTT/dEO4 is realized by the addition of LiTFSI, with the



material able to maintain smectic phases up to $r = [\text{Li}^+]/[\text{EO}] = 0.1$. The highest ionic conductivity of 8×10^{-3} S/cm was attained at an intermedium salt concentration of r = 0.05. It was also found that ion conduction in BTTT/dEO4 is enhanced by forming a smectic layered structure with irregular interfaces between the BTTT and EO4 layers and by the lateral film expansion upon salt addition. This can be explained by the enhancement of the misalignment and configurational entropy of the side chains, which increase their local mobility and that of the solvated ions. Our molecular design thus illustrates how, beyond the favorable energetic interactions that drive the assembly of ion solvating domains, modulation of entropic effects can also be favorably harnessed to improve ion conduction.

KEYWORDS: ion conduction, π -conjugated liquid crystal, molecular dynamics simulation, thin film electrochemical impedance spectroscopy, X-ray diffraction pattern

INTRODUCTION

Liquid crystals (LCs) are thermally stable mesophases whose properties lie between those of highly ordered crystalline phases and isotropic liquid phases. LCs are known for their spontaneous self-assembly behavior over large areas under mild conditions, which is induced by the segregation of immiscible components, in this case the rigid mesogenic conjugated oligothiophene cores and flexible oligo(ethylene oxide) tails.¹⁻³ By applying different molecular design strategies, nanostructured LCs may form well-defined 1D (columnar), 2D (lamellar), and 3D (bicontinuous cubic) nanochannels leading to efficient charge transport for electrochemical processes in potential applications in Li-ion batteries, 4,5 fuel cells, 6–8 organic transistors, 9,10 and solar cells. 11,12

The ionic conductivity in LC molecules is typically achieved by either ion-containing flexible polar or charged moieties. 5,13,14 More specifically, the ionic conduction of LCs can be obtained by use of a metal salt (e.g., lithium bis(trifluoromethanesulfonyl)imide, LiTFSI) dispersed in the polar phases and ion dissociation from adjacent charged moieties. 15,16 To induce electronic conductivity in LCs, the use of aromatic mesogens is a common strategy due to the

Received: August 4, 2022 Accepted: November 30, 2022 Published: December 7, 2022



ACS Nano www.acsnano.org Article

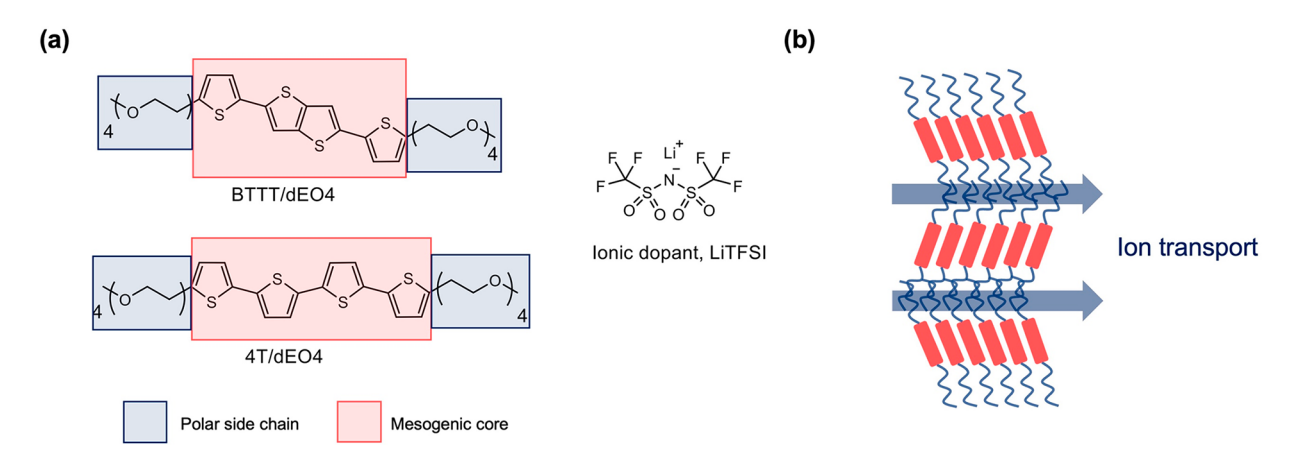


Figure 1. Molecular design of the liquid crystals. (a) Molecular structures of liquid crystals (BTTT/dEO4 and 4T/dEO4) and ionic dopants (LiTFSI) used to achieve ionic conduction characteristics. (b) Schematic illustration of ion transport in the layered morphology of BTTT/dEO4 and 4T/dEO4.

generation of strong noncovalent $\pi-\pi$ interactions. ¹⁷ In addition, suitable packing of mesogenic cores helps to enhance the nanophase segregation that drives the formation of different LC morphologies. The LC with a combination of ion- and electron-conducting functionalities is denoted as a mixed ionic/electronic conductor (MIEC). Polymer-based MIEC materials are usually associated with ambiguous structure—transport relationships due to the complex interplay of synthetic design, processing methods, and micromorphological control. ^{9,18,19} The examination of small molecules enables a computationally tractable model platform that efficiently provides additional microstructural details and physical insights that can be leveraged for designing polymeric MIECs. ^{20,21}

The induced electronic conductivity of LCs is commonly believed to be positively correlated with the organization of the overall structure. However, whether ionic transport has a similar correlation with the well-ordered mesophase structure of LCs remains unclear. Sakuda et al. studied the temperaturedependent anion conductivity of a cyclohexylphenyl-based LC in which the imidazolium cation functions as an ionconducting pathway. 14 The ionic conductivity increased smoothly with temperature when the LC entered the isotropic phase from the mesophase. Kuwabara et al. found that the Li⁺ conductivity of a bicyclohexyl-based LC with cyclic carbonate groups as conducting channels increased almost linearly with increasing temperature throughout the crystalline, LC, and isotropic liquid phases.⁵ However, the change of ionic conductivity as a function of temperature in a LC does not always follow the same trend. Verónica et al. studied the temperature-dependent K+ conductivities at elevated temperature in a LC containing a cyanobiphenyl mesogen and 18diazacrown ether as an ion-conducting component.²² The system showed a sudden drop in the K⁺ conductivities when the LC entered the isotropic liquid state, which was attributed to the disruption of structural alignment in the mesophase. These examples illustrate that the correlation between structural organization and ion-conducting properties in a LC is highly nontrivial and system-dependent.

In this work, we combined experimental and computational methods to investigate the complex relationship between the self-assembled mesophase structure and the ionic conductivity properties of a LC material. First, we have designed a synthetic pathway to produce a MIEC LC containing 2,5-bis(thien-2-

yl)thieno[3,2-b]thiophene (BTTT) as the mesogenic core attached with tetra(ethylene oxide) (EO4) at both ends, denoted BTTT/di-EO4 or BTTT/dEO4 for simplicity. Oligothiophene-based moieties are commonly used as the electron-conducting segment in organic electronics due to their well-known semiconducting properties,²³ and oligo-(ethylene oxide) often serves as the ion-conducting block due to its exceptional solvating ability of various metal salts.² Our previous study using quaterthiophene as a mesogenic core (4T/dEO4 in our notation) showed that ion conduction benefits from the formation of 2D ion transport channels.^{24–27} In the present work, we replaced the quaterthiophene by a fused thieno [3,2-b] thiophene having a more planar conformation to explore how the mesogenic chemistry changes the packing details and ion conducting properties of the ensuing mesophase.²⁸ The chemical structures of BTTT/dEO4, 4T/ dEO4, and the ionic dopant are shown in Figure 1a. Note that the motivation for synthesizing coil-rod-coil molecules is to leverage the formation of a layered morphology to further understand charge transport in the 2D channels of coil and rod domains parallel to the substrate, as illustrated in Figure 1b. We then optimized the fabrication process from the conventional "spin-cast" method to the "sit and cast" method to form LC thin films with uniform thickness and better quality. We examined the thermal behavior of BTTT/dEO4 and identified a mesophase with the lamellar structure from 15.7 to 71.5 °C. We adopted an integrated approach combining grazing incidence wide-angle X-ray scattering (GIWAXS) and molecular dynamics (MD) simulations to further reveal the molecular packing details in the self-assembly structure. Finally, we measured the ionic conductivities of BTTT/ dEO4 and compared them with those of the 4T/dEO4 molecule. Overall, BTTT/dEO4 has higher ionic conductivity than that of 4T/dEO4 at all Li-salt concentrations, but the most significant ionic conductivity difference was observed at r = 0.1 ($r = [Li^+]/[EO]$). The maximum ionic conductivity of BTTT/dEO4 is 8.23×10^{-3} S/cm at r = 0.05 at 100 °C.

RESULTS AND DISCUSSION

Thermal and Structural Properties of BTTT/dEO4. To understand the thermal behavior of LC BTTT/dEO4, we employed thermogravimetric analysis (TGA), differential scanning calorimetry (DSC), temperature-dependent wideangle X-ray scattering (T-WAXS), and polarized optical

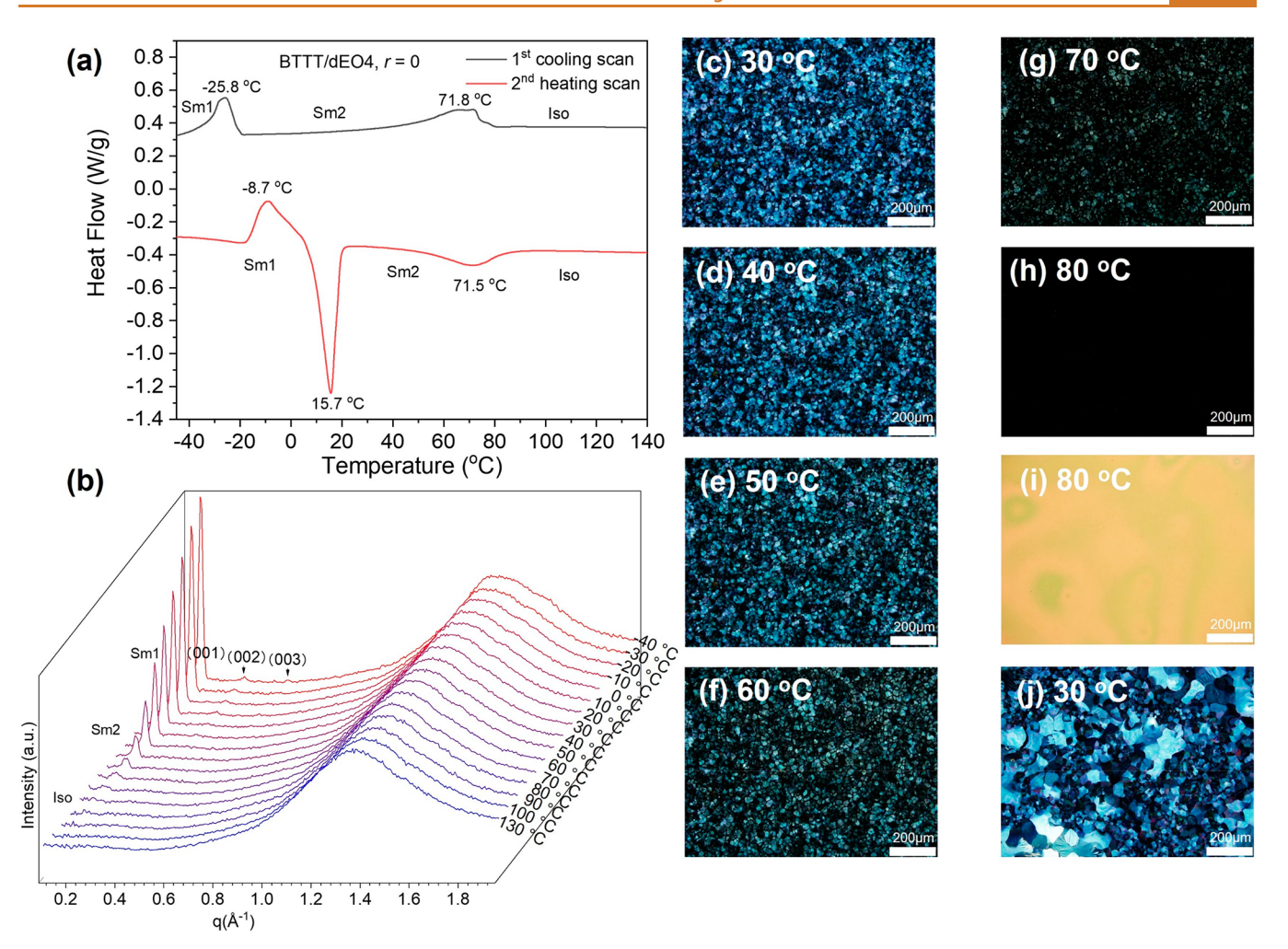


Figure 2. Self-assembly and thermal behaviors of BTTT/dEO4. (a) Differential scanning calorimetry (DSC) traces of BTTT/dEO4 at a 10 °C/min cooling and heating rate. Sm1 = smectic phase 1, Sm2 = smectic phase 2, and Iso = isotropic. (b) Wide angle X-ray scattering (WAXS) profiles of BTTT/dEO4 from -40 to 130 °C. The broad peak from 1.0 to 1.8 Å⁻¹ is primarily from the capillary used in the WAXS measurement. (c-h) Polarized optical microscopy (POM) images of BTTT/dEO4 heated from 30 °C (smectic phase) to 80 °C (isotropic phase). (i) Optical image of BTTT/dEO4 at 80 °C. (j) POM image of BTTT/dEO4 annealed from 80 to 30 °C.

microscopy (POM). TGA measurements demonstrated the thermal stability of BTTT/dEO4, while DSC showed distinct transition states of the LC. T-WAXS measurements were performed to understand the structural information (e.g., layered morphology) of the LC at different temperatures, and POM images were taken to verify the formation of the LC and thermal transitions of the LCs at different temperatures. The onset decomposition temperature for BTTT/dEO4 is 284 °C, as measured by TGA (see Figure S4). All characterization was performed below this decomposition temperature. For neat BTTT/dEO4, there are one exothermic and two endothermic events in the second heating scan of DSC as shown in Figure 2a. The compound exhibits a smectic LC phase (Sm1) below 15.7 °C and an exothermic peak at −8.7 °C that reflects a cold ordering or cold crystallization event. The cold crystallization event during the heating scan happens when the semicrystalline material is unable to fully crystallize under the cooling conditions.²⁹ DSC measurements with different heating and cooling rates (Figure S5) were performed to detect the kinetics of cold crystallization behavior. The resulting thermal properties for cold crystallization are shown in Table S1. As the heating/cooling rate increases, the enthalpy for cold crystallization decreases and the cold crystallization temperature $(T_{\rm cc})$ increases. It is easier for the compound to recrystallize at a lower scan rate, and the resulting degree of crystallization after $T_{\rm cc}$ is also higher. The compound exhibits a second smectic (Sm2) LC phase between 15.7 and 71.5 °C with the endothermic peak at 71.5 °C associated with the transition temperature between the LC phase and isotropic (Iso) phase.

Structural information related to the thermal transitions of the BTTT/dEO4 LC was investigated by coupling DSC traces with T-WAXS. T-WAXS data were collected from -40 to $130\,^{\circ}\text{C}$, and three clear states can be found in Figure 2b. From -40 to $20\,^{\circ}\text{C}$, BTTT/dEO4 is in the Sm1 phase and three peaks with a d-spacing ratio of 1:1/2:1/3 are present, which are assigned as (001), (002), and (003). The formation of a smectic layered structure is confirmed by the periodic peaks, and the interlayer distance in BTTT/dEO4 is $36.5\,$ Å. The system transits to the Sm2 phase and loses some of its long-range order for layer packing (as marked by the disappearance of peaks (002) and (003)) between 20 and 70 °C. Yeates et al. measured the melting temperature $(T_{\rm m})$ of ethylene glycol oligomers and found that the $T_{\rm m}$ of the oligomer with 15 repeating units is 40 °C and the $T_{\rm m}$ of the oligomer with nine repeating units is $30\,^{\circ}\text{C}$. For the BTTT/dEO4, the

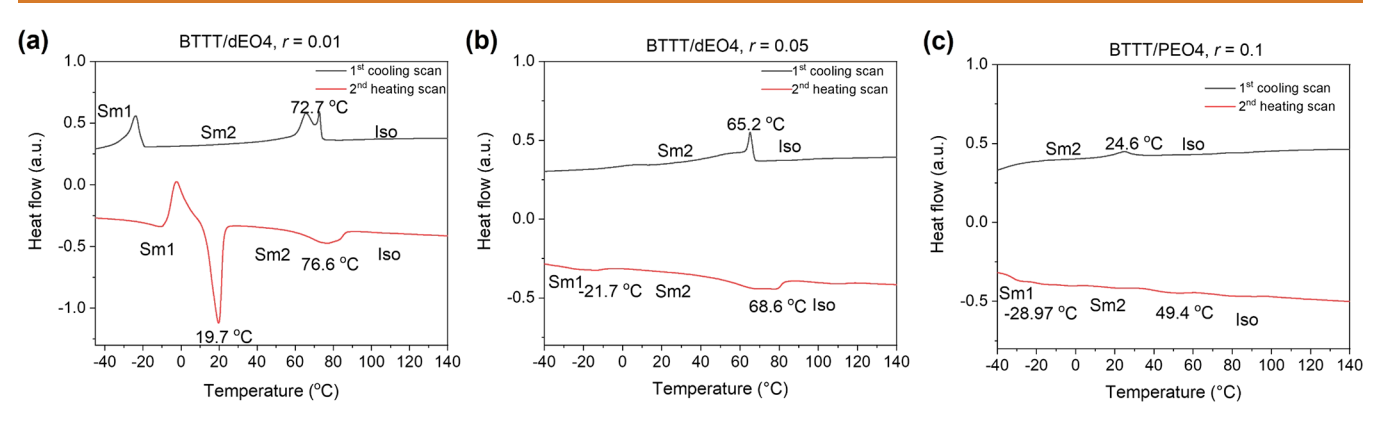


Figure 3. DSC thermograms for BTTT/dEO4 blended with different salt concentrations measured at a scanning rate of 10 $^{\circ}$ C/min. (a) r = 0.01, (b) r = 0.05, (c) r = 0.1. Sm1 stands for smectic phase 1, Sm2 stands for smectic phase 2, and Iso stands for isotropic.

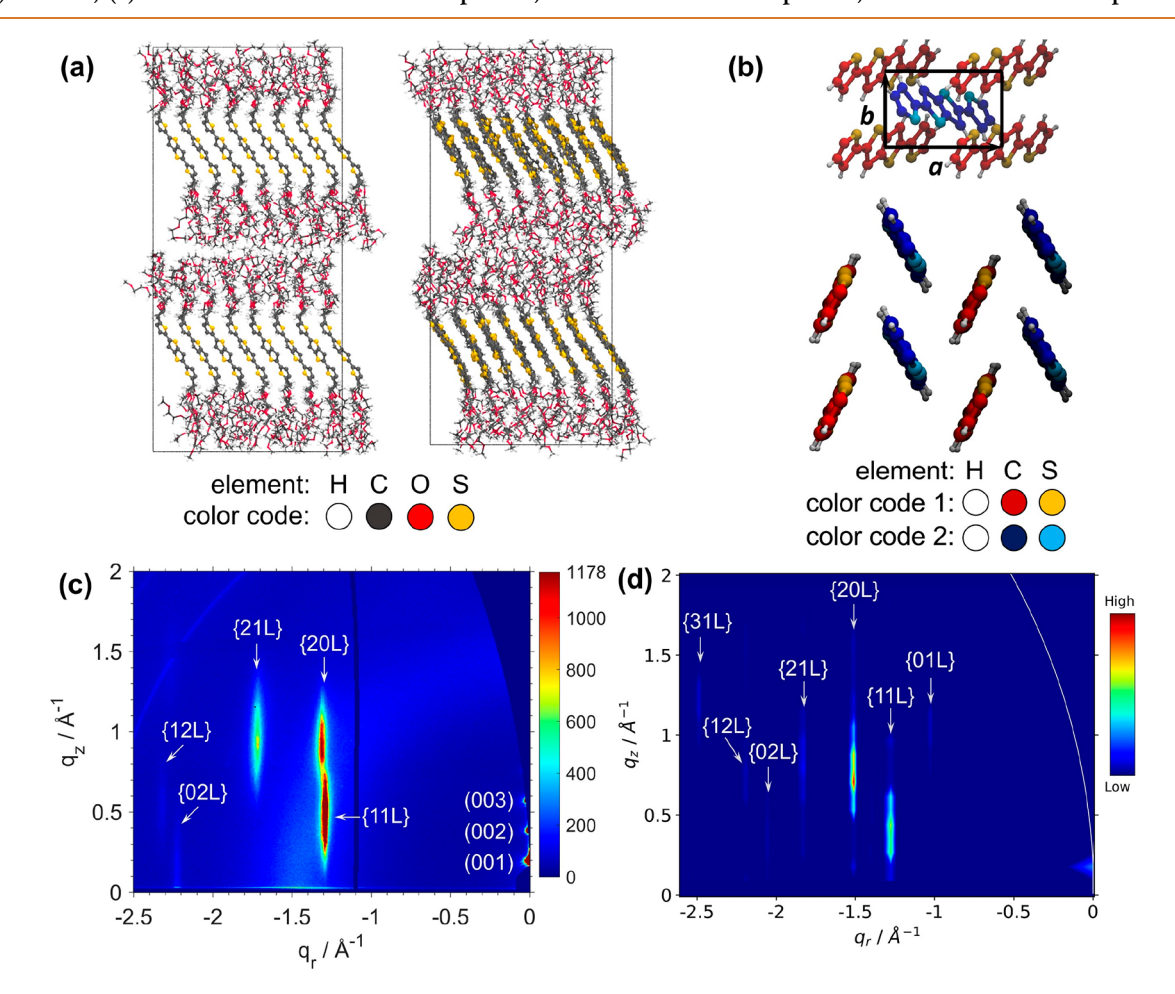


Figure 4. GIWAXS indexing of BTTT/dEO4. (a) Snapshots of the initial crystal configuration (left) and thermally equilibrated configuration at 300 K (right) for BTTT/dEO4. (b) Illustration of redefined in-plane lattice vectors (top) and in-plane molecular orientations in the herringbone motif (bottom). For clarity, only the BTTT segment is displayed. The two molecular orientations are colored based on different color code sets. In each color code set, atoms are colored based on chemistry. (c) Experimental GIWAXS pattern of the BTTT/dEO4 thin film at r = 0. (d) Simulated GIXD pattern of thermally equilibrated configuration. Intensities in (c) and (d) are shown on a linear scale. Miller indices are provided for most of the intense vertical Bragg rods.

endothermic peak at 15.7 $^{\circ}$ C most likely corresponds to the melting of the EO4 side chains. This melting would allow the EO4 side chains to have greater mobility and more varied conformations. As the temperature increases from 20 to 70 $^{\circ}$ C, the intensity of the primary peak gradually decreases and becomes featureless after 70 $^{\circ}$ C, signaling a transition from the Sm2 phase to the Iso phase.

POM was used to provide direct evidence for the formation of the LC phase with an optimized "sit and cast" fabrication process. A description of the optimization process (Figures S6–S10) can be found in Supporting Information S3. The compound was heated from 30 to 80 °C and then cooled from 80 °C back to 30 °C. POM images were taken to monitor the phase transitions during thermal treatment. Figure 2c—h shows

the evolution of POM images as the compound was heated from 30 to 80 °C. The color in POM images gradually becomes darker as the temperature increases and becomes completely dark at 80 °C, indicating the transition of the compound from the smectic phase to the isotropic phase. Also, the LC was fully melted at 80 °C, and the thin film sample did not dewet from the substrate, as confirmed by optical images in Figure 2i. As the compound was cooled from 80 to 30 °C, the LC phase was recovered as shown in Figure 2j.

To better understand the phase behaviors of the compound upon salt addition, the BTTT/dEO4-LiTFSI complex with different blending ratios $(r = [Li^+]/[EO])$ was investigated by DSC (see Figure 3); the correlated thermal properties are shown in Table S2. The compound was able to maintain a uniform smectic LC phase with salt concentrations up to r =0.05. Comparing BTTT/dEO4 at r = 0 and r = 0.01, the addition of small amounts of salt aids the formation of an ordered LC phase, evidenced by the increased enthalpy for the transition from the Sm2 phase to the isotropic phase during the heating scan as well as the increased enthalpy for the transition from the isotropic phase to the Sm2 phase in the cooling scan. At r = 0.05, the order found for the compound in the LC phase decreases and the DSC trace becomes almost featureless at r = 0.1, indicating the disruption of the LC order. The addition of LiTFSI also causes film expansion. A detailed discussion can be found in the GIWAXS section.

In summary, BTTT/dEO4 LC exhibits one exothermic and two endothermic events (Sm1, Sm2, and Iso) from -40 to 140 °C, as evidenced by DSC and T-WAXS. POM verifies the thermal transition between the Sm2 phase and Iso phase and shows that the film can uniformly cover the substrate during the heating and cooling scans. While the above characterizations allow us to correlate the thermal behaviors with the sample morphologies, we will combine experimental GIWAXS and molecular dynamics simulations to gain deeper insight into the molecular packing of the LC phases.

Molecular Packing of BTTT/dEO4. As a dual-phase conducting material, BTTT/dEO4 molecules contain both rigid electron-conducting segments (the BTTT segments), which usually form highly ordered solid-like nanodomains, and flexible ion-conducting blocks (the EO4 segments), which form less ordered liquid-like nanodomains. The complex semicrystalline nature of these thin films poses a challenge for extracting useful molecular packing information from limited and incomplete X-ray diffraction (XRD) data. MD simulation provides a useful complementary modeling approach to identify hypothetical structures whose XRD patterns could be qualitatively or semiquantitatively consistent with experimental data. Known crystal structures of relevant chemical species were used as templates to generate the initial hypothetical crystal configuration. All-atom MD simulations were then performed at the selected temperature (see Supporting Information S4) to relax the structure and allow for atomic thermal vibrations to take place. This thermal equilibration process, however, only allows for limited rearrangement of molecular orientations within the time scale of the simulations, leading to configurations which, while only an approximation to the most stable molecular packing structure, are adequate to capture essential features of the expected XRD patterns. Indeed, the simulated configuration is used to calculate the corresponding XRD pattern under the grazing-incidence X-ray diffraction (GIXD) framework (see Supporting Information S5) to complement the

experimental GIWAXS characterization. Furthermore, different purposely designed initial configurations can be used to investigate how the GIXD pattern changes with certain spatial features of the simulated configuration, a strategy that we later exploit to explain experimental XDR features.

The α -quaterthiophene high-temperature polymorph (α -4T/HT)³¹ was selected as a template to generate the initial crystal configuration (see Supporting Information S6.1), which was then equilibrated at 300 K to form a lamellar structure (see Figure 4a). The herringbone packing motif was embedded in the BTTT layers of our initial simulation configuration and was preserved during the thermal equilibration process. For our ensuing discussion, the following notation of lattice vectors (a, b, c) is used for structures featuring the herringbone motif (see Figure 4b): the a-axis is defined as the stacking direction of the molecule-column with the face-to-edge arrangement, the b-axis is defined as the packing direction of molecules in the same column with the face-to-face arrangement, and the c-axis is defined as the lamella stacking direction. For the lattice parameters, a is the distance between two molecules with the same orientation for every other column, and b is the distance between two adjacent molecules in the same column. Note that the convention of $a \ge b$ is adopted, which is more intuitive in defining the unit cell (see Figure S16b,d).

The GIXD pattern is normally plotted in a space spanned by q_r (the in-plane component of the scattering vector, parallel to the substrate/film) and q_z (the out-of-plane component, perpendicular to the substrate/film). The calculation of the simulated GIXD pattern usually requires some guiding information from the experimental results, which we now outline. Figure 4c shows the measured GIWAXS pattern of a BTTT/dEO4 thin film. The diffraction intensity is scaled by its maximum value in the pattern to take into account the intensity dependence of the sample geometry and the instrumental setup. All the diffraction peaks are well grouped by discrete in-plane q_r values, which are known as vertical Bragg rods. The presence of vertical Bragg rods indicates the formation of 2D-powder polycrystallites in the film, i.e., one specific crystal plane of all crystallites is parallel to the substrate, while the in-plane orientations of these crystallites are largely isotropic. A series of peaks is found along the edge of $q_r \approx 0$ in the GIWAXS pattern, indicating that molecules in the film are aligned in an edge-on configuration and the lamella stacking direction is perpendicular to the substrate. In the edge-on configuration, the a-b plane of the lattice is parallel to the film, the same as the x-y plane.

Consistent with the film setup of 2D-power polycrystallites and the edge-on alignment, a representative simulated GIXD pattern was calculated using an equilibrated configuration (see Figure 4d). In this simulated pattern, most of the intense Bragg rods are labeled with their respective Miller indices. The Miller indices (*hkl*) are defined accordingly using the reciprocal lattice vectors; the Miller indexed vector is defined by

$$G_{hkl} = ha^* + kb^* + lc^* \tag{1}$$

The in-plane Miller indices refer to h and k, and the out-ofplane index refers to l. The Miller indexed planes are used to refer to the family of parallel lattice planes orthogonal to G_{hkl} . The interplanar spacing between adjacent lattice planes is the same and given by

$$d_{hkl} = \frac{2\pi}{|\mathbf{G}_{hkl}|} \tag{2}$$

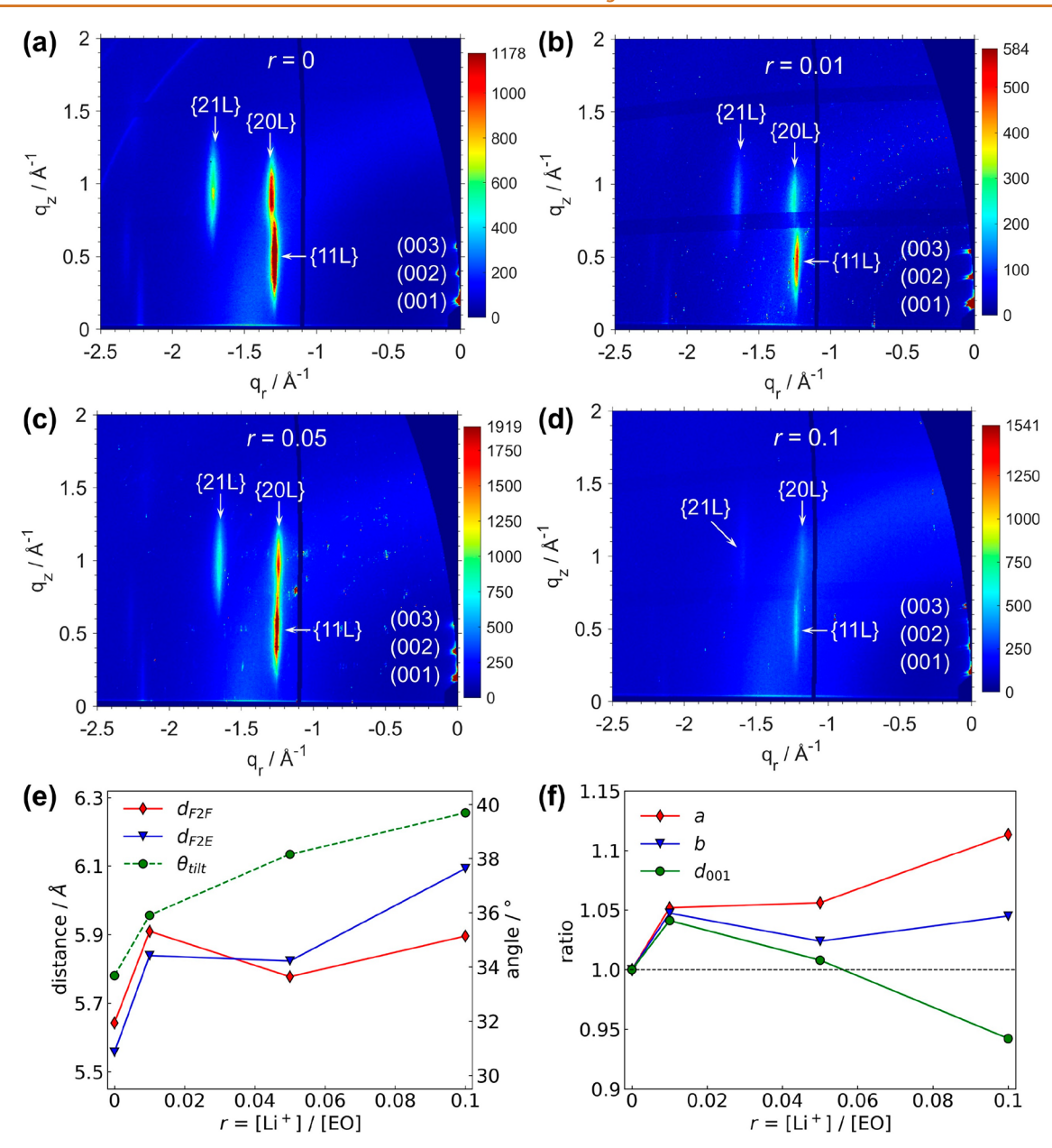


Figure 5. Experimental GIXD patterns of BTTT/dEO4. (a-d) GIXD pattern of the BTTT/dEO4 films at different salt concentrations. Intensities are shown on a linear scale. The film expansion behavior is characterized through (e) distances between neighboring molecules with face-to-face arrangement ($d_{\rm F2E}$), face-to-edge arrangement ($d_{\rm F2E}$), and molecule tilt angle ($\theta_{\rm tilt}$), and (f) in-plane lattice parameters (a and b) and the out-of-plane Miller indexed spacing ($d_{\rm 001}$).

The notation $\{hkl\}$ denotes the set of all Miller indices that are equivalent to (hkl) by the symmetry of the lattice. The Miller indexed rod is used to mark the vertical Bragg rod with specified in-plane Miller indices and unspecified out-of-plane Miller index. In general, the well-defined in-plane Miller indices can reveal many packing details within the film plane (the x-y plane in our setup), while the out-of-plane linecut profile (along q_z) of the vertical Bragg rods can provide structural information in the direction normal to the film (the z-direction).

In-Plane Miller Indices Reveal a Two-Particle Unit Cell and a Herringbone Motif within the Film Plane. In the film plane, several relationships between packing features and in-plane Miller indices are established by coanalyzing the simulated configuration and its GIXD pattern. A single rod without splitting is found at {11L}, {21L}, {12L}, and {31L},

each of which has possible multiplicities. This is consistent with the fact that the angle between a and b is 90° in the simulated configuration. Otherwise, the $\{11L\}$ rod should split into two separate rods of $\{11L\}$ and $\{1\underline{1}L\}$, where $\underline{1}$ represents -1. The presence of $\{11L\}$, $\{20L\}$, $\{02L\}$, and $\{31L\}$ confirms a two-dimensional centered rectangular lattice and is consistent with two molecules per unit cell. Moreover, the appearance of $\{01L\}$, $\{21L\}$, and $\{12L\}$ stems from the two distinct molecular orientations in the herringbone motif (see Supporting Information S6.2), which can be approximately regarded as p2gg symmetry. Note, however, that the low symmetry of BTTT makes it impossible to arrange two molecules in the unit cell with two glide symmetry planes.³²

Molecular Tilt Angle Can Be Estimated from Peak Positions of Vertical Bragg Rods. In the direction normal to the film, the semicrystalline nature of BTTT/dEO4 films

ACS Nano www.acsnano.org Article

significantly complicates their structural characterization. The disordered region of EO segments can create translational and rotational mis-registration between adjacent molecular layers³³ and make the c-axis of the lattice unit cell ill-defined. Nevertheless, based on our simulations, we developed an approach to estimate the molecular tilt toward the film by taking advantage of the rigid, rod-like shape of the BTTT segment and defining a molecular tilt angle (θ_{tilt}) as the angle between the end-to-end vector of BTTT and the normal direction of the film. This molecular tilt angle can be calculated using the diffraction peak positions of selected vertical Bragg rods based on specific assumptions as described in Supporting Information S6.3. The linecut profile of each vertical Bragg rod along q_z can be used to obtain its peak position. We note that peak intensities are usually needed to extract molecular packing details inside the unit cell, and hence our approach based only on peak positions is less precise. However, determination of peak intensities is difficult and largely impractical for some of our experimental GIWAXS patterns. In contrast, the peakposition-based molecular tilt angle can be calculated from most of our experimental patterns and serves as a semiquantitative parameter to track some structural changes under different conditions. Although our approach was developed for rod-like molecules in a 2D centered rectangular lattice, we surmise that a similar calculation can be derived for other lattice types.

We can use the experimental GIWAXS pattern in Figure 4c to illustrate the application of our simulation analysis (see Supporting Information S6.4) and to estimate the molecular tilt angle as 33.7°. Comparing the experimental and simulated GIXD patterns in Figure 4, while reasonable agreement is indeed observed in the peak indices, several minor discrepancies exist, especially in terms of the exact peak positions. These observations suggest that the nature of the film packing structure is largely captured by the simulated configuration, whereas packing details including lattice parameters and the molecular orientation need further refinement. Importantly, the analysis framework developed from simulated structures is sufficient to extract fruitful structural information directly from experimental GIWAXS patterns.

BTTT Segments Rearrange Their Positions and Orientations upon Salt Addition. To study the effect of the Li-salt on the film structure, GIWAXS was measured on BTTT/dEO4 films with different salt concentrations, and the diffraction intensity in each pattern was scaled by its own maximum value (see Figure 5a-d). Based on our analysis framework, the Bragg rods of {11L}, {20L}, and {21L} were identified in each pattern, indicating that the herringbone packing motif was maintained by the BTTT segments in the presence of the lithium salt. While the position and intensity of these Bragg rods change across different patterns, our analyses focus on the diffraction peak positions. The addition of lithium salt induced shifts in the positions of Bragg rods, suggesting that the BTTT segments experienced some positional and orientational rearrangements. To quantify these molecular rearrangements, we examined and tracked three parameters: the distance between neighboring BTTT segments with the same orientation (i.e., adopting the face-to-face arrangement), $d_{\rm F2F}$, the distance between neighboring BTTT segments with different orientations (i.e., adopting the face-to-edge arrangement), d_{F2E} , and the molecular tilt angle mentioned earlier, θ_{tilt} . These two distances are calculated from the in-plane lattice parameters,

$$d_{\text{F2F}} = b, \quad d_{\text{F2E}} = \frac{1}{2}\sqrt{a^2 + b^2}$$
 (3)

Note that $d_{\rm F2F}$ and $d_{\rm F2E}$ are the in-plane translational distance between neighboring BTTT segments, which are not equivalent to the shortest distance between two segments due to the molecular inclination toward the film plane. It is nontrivial to obtain this shortest distance in our system due to the ill-defined c-axis. In contrast, $d_{\rm F2F}$ and $d_{\rm F2E}$ are more accessible and reliably calculated from the experimental patterns at different conditions. The software GIXSGUI³⁴ was used to locate peak positions in the experimental GIWAXS patterns, and the parameters mentioned above were calculated accordingly (see Figure 5e). When the lithium salt was added into the film, it is expected to be mainly located in the EO4 layers. The adjacent EO4 segments from different molecules must then spread out to form coordinating environments to accommodate the Li-ions, generating local stresses that propagate to the BTTT segments, and lead to the increase of d_{F2F} and d_{F2E} . As the salt concentration increases, d_{F2E} shows a larger increment than $d_{\rm F2F}$, indicating a weaker interaction between neighboring BTTT segments with the face-to-edge arrangements. Concurrently, the enlarged in-plane distance between neighboring BTTT segments leads to a larger molecular tilt angle to maintain the effective $\pi - \pi$ stacking between segments. A similar trend of structural change was also found in the simulations with different salt concentrations (see Supporting Information S6.5).

Anisotropic Film Expansion Is Observed upon Salt **Addition.** Three characteristic lengths were used to track the film expansion behavior, including the in-plane lattice parameters a and b and the out-of-plane Miller indexed spacing d_{001} . Due to the ill-defined c-axis in our system, we need to clarify that G_{00L} (the corresponding Miller indexed vector of d_{00L}) refers to vectors only having the out-of-plane component, i.e., $q_r = 0$ and $q_z \neq 0$. Since a, b, and d_{001} are defined in three orthogonal directions (a, b, G_{001}) , these lengths allowed us to investigate the anisotropy of the film expansion. For this comparison, all the characteristic lengths were scaled by their corresponding values in the neat film without any Li-salt (see Figure 5f). For the in-plane directions, the BTTT/dEO4 layer expands more along a than along b as the salt concentration increases, indicating a preferred and favorable direction for the molecules to positionally rearrange. For the out-of-plane direction, the spacing d_{001} , which can be regarded as the molecular layer thickness, initially increases and then decreases with salt concentration, a trend that can be explained by the fact that the required out-of-plane expansion upon salt addition was counteracted by the increasing molecular tilt (θ_{tilt}) toward the film.

Intensity Changes in GIWAXS Pattern Suggest Decreasing Order of BTTT Layers upon Salt Addition. Typically, the intensity change in the GIWAXS pattern is related to the packing details in relatively perfect crystallites and the lattice disorder caused by random displacements of individual molecules. In our case, the presence of disordered EO4 layers embedded in the BTTT/dEO4 crystallites makes the interpretation of the intensity information more complicated. Among the Bragg rods identified in our experimental patterns, the (00L) rod is associated with the lamellar structure, for which an analysis of peak intensity is relatively straightforward. A detailed discussion on the correlation between the lamellar structure and ionic con-

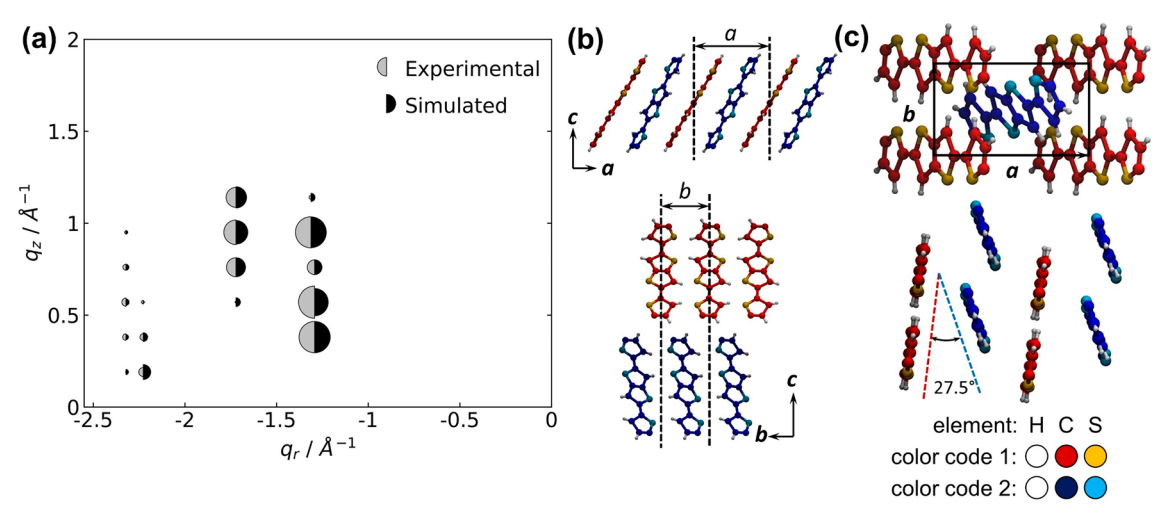


Figure 6. Molecular arrangement of BTTT/dEO4. (a) The experimental and simulated GIXD intensities of a BTTT/dEO4 film without lithium salt doping, r = 0. The diffraction intensity is indicated by the area size of a half-circle. (b) Out-of-plane packing motifs of the best-fit molecular alignment for the BTTT segments obtained from the crystallographic refinement, which is illustrated by the structure viewed along the b-axis and a-axis. Molecules with same orientation form a so-called molecule-column. Differently orientated molecules are colored in two color code sets, with atom color based on elemental chemistry in each color set. Snapshots are cropped around the layer of BTTT segments. In the b-c plane, molecular columns with different orientations are shown separately for comparison, and their relative distance along the c-axis is cropped and does not reflect their actual positions. The molecular tilt angles are 31.3° for the BTTT segments colored in red and 26.4° for the BTTT segments colored in blue. (c) In-plane packing motifs of the best-fit molecular alignment for the BTTT segments, which is illustrated by the structure viewed along the c-axis with in-plane lattice vectors and along the molecular long-axis for easy viewing of different molecular orientations.

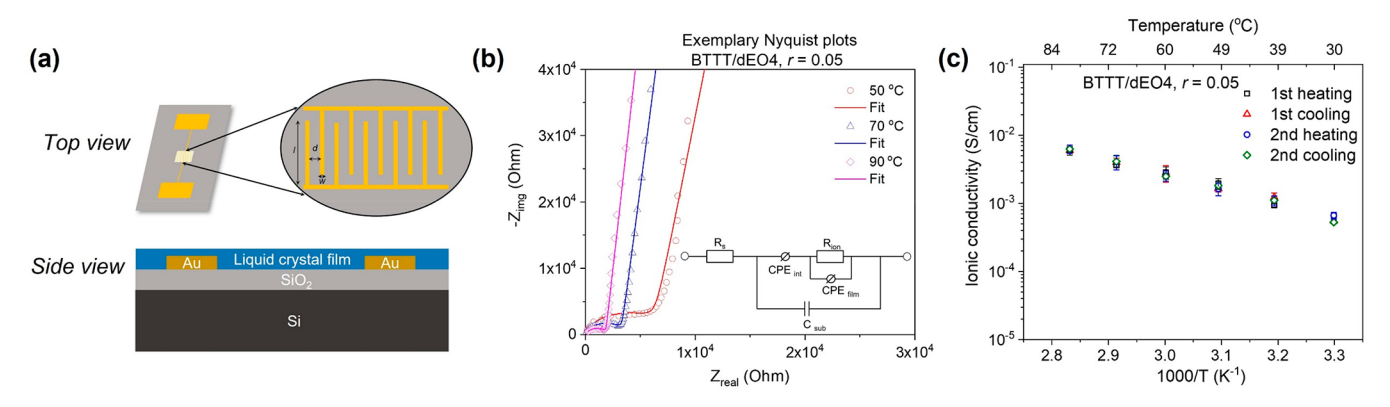


Figure 7. Thin film electrochemical impedance spectroscopy. (a) Schematic illustration of interdigitated electrode array with deposited liquid crystal thin film. (b) Exemplary Nyquist plots of BTTT/dEO4 at r = 0.05 with inserted equivalent circuit used to extract film resistance. (c) Temperature-dependent ionic conductivities of BTTT/dEO4 at different heating and cooling scans.

ductivity is given in the next section. The Bragg rods of {11L}, {20L}, and {21L} are related to more complicated in-plane structural details such as the orientation and stacking of the planar BTTT segments. A plausible analysis of their intensity data would require the introduction of rather restrictive assumptions, which would be difficult to validate in some of our experimental patterns; hence, only a preliminary interpretation is provided. The salt-induced in-plane film expansion mentioned earlier can create extra room to allow larger displacements of BTTT segments, facilitating the formation of defects and distortions that disrupt the BTTT lattice structure. Thus, we conjecture that as salt concentration increases, the declining relative intensities of {11L}, {20L}, and {21L} are largely due to the decreasing order in the BTTT layers.

Lastly, a crystallographic refinement using the diffraction intensities was implemented based on three assumptions (see below). This refinement can provide some additional

information related to the alignment of the BTTT segment in the unit cell, beyond the peak-position-based analysis presented before. However, to get a reliable outcome, the refinement was restricted to cases exhibiting strong and distinct diffraction peaks, and thus it only provided additional details which did not affect the main properties of interest. The three assumptions adopted were as follows: (i) An orthorhombic unit cell was selected, and the length of the c-axis was set to be the spacing for the (001) Miller indices, d_{001} , to handle the illdefined c-axis in our system. (ii) Only the BTTT segments were included in the refinement due to their highly ordered packing. We note that the contribution of segmental interference to the diffraction intensity could be missed by artificially "removing" the EO4 segments. (iii) The BTTT segments were treated as rigid objects to drastically reduce the number of fitted degrees of freedom, thus allowing the use of the limited and incomplete diffraction peaks in the experimental patterns. This assumption of rigid molecules

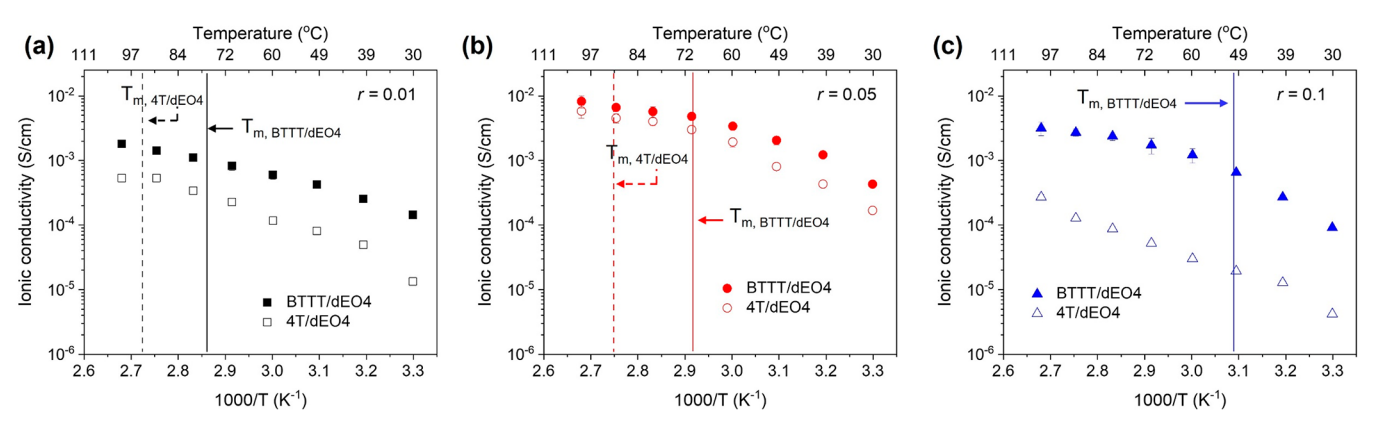


Figure 8. Temperature-dependent ionic conductivities of BTTT/dEO4 and 4T/dEO4. Ionic conductivities of BTTT/dEO4 and 4T/dEO4 at different salt concentrations, (a) r = 0.01, (b) r = 0.05, and (c) r = 0.1. The solid line reflects the melting temperature of BTTT/dEO4, and the dashed line reflects the melting temperature of 4T/dEO4. Note that the melting temperatures of 4T/dEO4 at different r values are obtained from our previous report. 24

ı

has been used for several systems involving aromatic molecules. 32,33,35 The crystallographic refinement was performed by minimizing the residual between experimental and simulated intensities, and is applied to the case of neat film in Figure 5a. Integrated intensities were measured at 17 distinct peaks after proper background removal using GIXSGUI.³⁴ The lattice parameters were calculated and set to be a, b, c, α , β , γ = 9.58 Å, 5.64 Å, 33.07 Å, 90°, 90°, and 90°. Centers of mass of two BTTT segments in the unit cell were fixed at the fractional positions of [0, 0, 0] and [0.5, 0.5, 0]. Six degrees of freedom were considered in the refinement: three Euler angles for each BTTT segment. The numerical minimization was achieved using Monte Carlo Simulated Annealing³⁶ combined with parallel tempering³⁷ (see Supporting Information S6.6). The best-fit simulated and experimental data are shown in Figure 6a, and the corresponding molecular arrangement displays the typical herringbone packing motif in Figure 6b,c. The molecular tilt angles (θ_{tilt}) of these two orientations are 31.3° and 26.4°, and the dihedral angle enclosed by two molecular planes with different orientations is 27.5°.

Ionic Conductivities of BTTT/dEO4 and 4T/dEO4. Inplane (lateral) ion conduction in the BTTT/dEO4 and 4T/ dEO4 LC thin films was probed by electrochemical impedance spectroscopy (EIS) measurements. LC thin films were deposited on top of custom-fabricated interdigitated electrodes (IDEs) through an optimized "sit and cast" method (see Supporting Information S3) to yield stable films for high signal-to-noise EIS. 38-40 Figure 7a shows the schematic top and side view of the IDE with the LC film coated on the substrate. POM images of doped BTTT/dEO4 and 4T/dEO4 on top of IDE are used to confirm the presence of a LC mesophase. For BTTT/dEO4 birefringence decreases at r = 0.05 and becomes featureless at r = 0.1, while for 4T/dEO4 birefringence can be preserved up to r = 0.1 (see Figure S11). T-WAXS and GIWAXS patterns confirm that both BTTT/dEO4 and 4T/ dEO4 form edge-on, layered structures (layers are parallel to the substrate) with one electron-conducting layer (thiophene core) and one ion-conducting layer (oligoethylene oxide side chain). 24,41 Furthermore, GIWAXS experiments were performed at two different grazing angles ($\theta = 0.08$ and 0.12) for BTTT/dEO4 films at r = 0.05 to examine the structure at different depths, especially the region close to the surface.⁴² The results show that BTTT/dEO4 is able to maintain the layered structure (marked by the presence of (001), (002), and

(003) peaks) in the top 6 nm of the film close to the surface, which is consistent with the rest of the film (see Figure S39 in Supporting Information S7.3).

Figure 7b shows the representative Nyquist plots for BTTT/ dEO4 at r = 0.05 and the applied equivalent circuit model to extract ionic film resistance. The Nyquist plots for BTTT/ dEO4 obtained at r = 0.05 and different temperatures consist of one semicircle and one capacitive tail, indicating the resistive and capacitive behaviors of ion transport. The diameter of the semicircle corresponds to the ionic resistance (R_{ion}) . As temperature increases, the diameter of the semicircle in Nyquist plots decreases, suggesting a faster ion transport event in the LC film. The representative Nyquist plots for BTTT/dEO4 at r = 0.01 and 0.1 are shown in Figure S12. Temperature-dependent conductivity measurements with multiple heating and cooling scans were performed to examine the thermal stability of LC thin films (shown in Figure 7c). The sample was first heated to 100 °C and cooled to 30 °C, followed by two heating and two cooling scans. All conductivities extracted from the equivalent circuit from different scans overlapped with each other, indicating that the film was not dewetted from the gold electrodes during the heating and cooling processes. In addition, ionic conductivities of BTTT/dEO4 at r = 0.05 were also measured with film thickness from 10.5 to 128.7 nm (see Figure S13). Ionic conductivities of BTTT/dEO4 show no dependence on film thickness in this range.

To probe the ion transport in BTTT/dEO4 and 4T/dEO4 films, EIS was performed at different salt concentrations and temperatures (see Figure 8, Figure S14). Ionic conductivities of both LCs increase with temperature, the result of a thermally activated conducting mechanism. 43-45 As the salt concentration increases from r = 0.01 to r = 0.05, the ionic conductivities of both LCs also grow due to the increase of ionic carriers. However, as the amount of salt increases further from r = 0.05 to r = 0.1, the ionic conductivities of both LCs decrease, which is related to the smaller dissociation ratio of LiTFSI and the slower motion of ethylene oxide chains caused by their cross-links with Li-ions. 20 Overall, the highest ionic conductivity for BTTT/dEO4 is 8×10^{-3} S/cm at r = 0.05 and 100 °C and that for 4T/dEO4 is 5.8×10^{-3} S/cm under the same conditions. Furthermore, compared to 4T/dEO4, BTTT/dEO4 shows higher ionic conductivities at all conditions we measured. At r = 0.01 and 0.05, the ionic

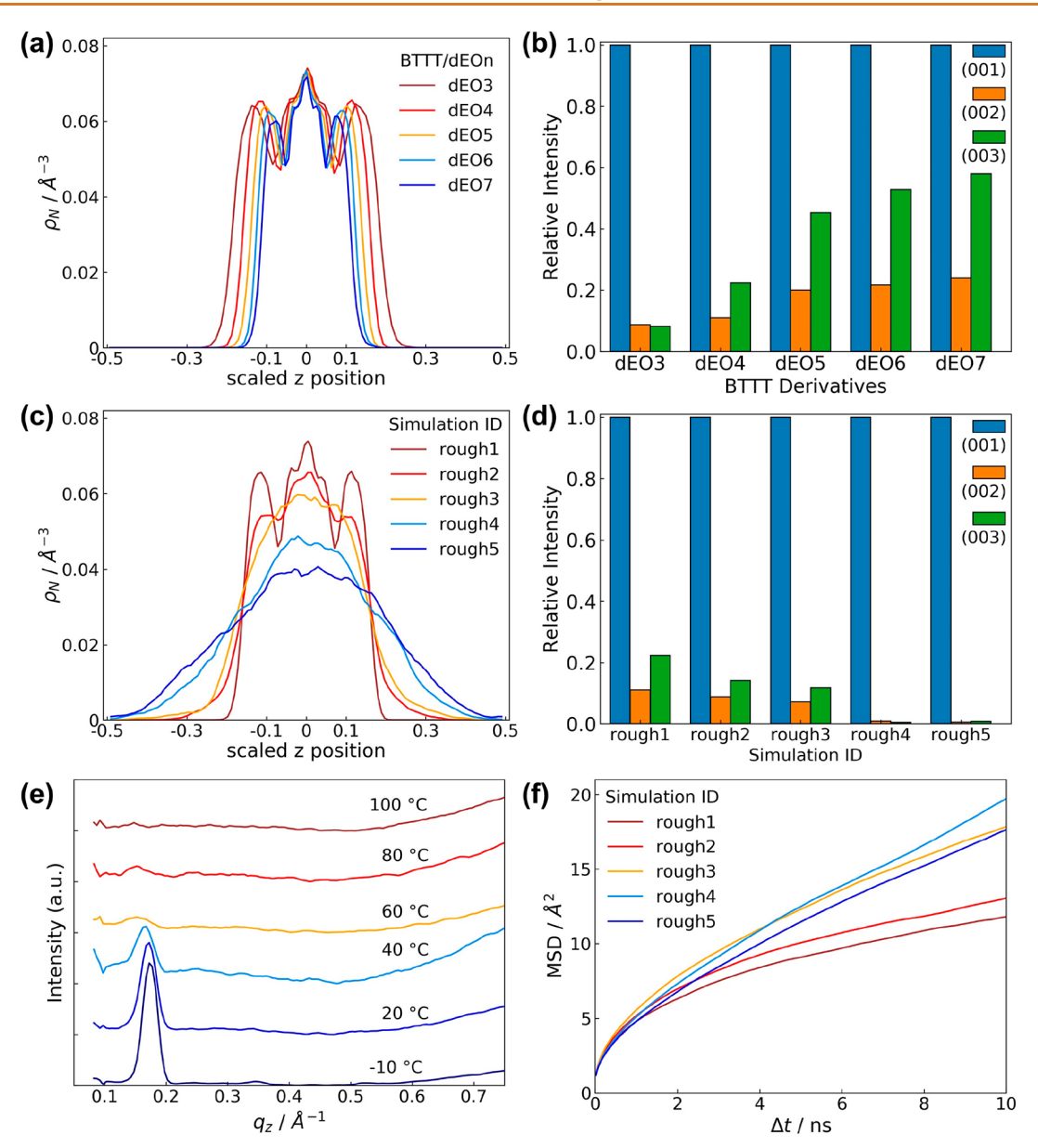


Figure 9. Layered structure of BTTT/dEO4. (a) Number density profiles along the z-direction, and (b) relative intensity profiles of the (00L) peaks for BTTT/dEOn derivatives with the layered structure obtained from simulated configurations. (c) Number density profiles along the z-direction, and (d) relative intensity profiles of the (00L) peaks for simulated BTTT/dEO4 configurations with different interfacial roughness between the BTTT and EO4 layers. (e) Representative experimental WAXS curves of the neat BTTT/dEO4 film at different temperatures obtained from Figure 2b. (f) MSD plots of the EO4 segment in the simulated BTTT/dEO4 configurations with different interfacial roughness.

conductivities of BTTT/dEO4 are slightly higher than those of 4T/dEO4. For r=0.1, the highest ionic conductivity of BTTT/dEO4 is 11.7 times higher than that of 4T/dEO4. In addition, the ionic conductivity of BTTT/dEO4 with 2D lamellar conducting channels is 2.05×10^{-3} S/cm at r=0.05 and 40 °C. In a study of zwitterionic LCs at the same temperature, the optimal ionic conductivity in 1D cylinder channels and 3D bicontinuous cubic channels are ca. 5×10^{-8} and 5×10^{-7} S/cm, respectively. Apart from the different LC chemistries involved, it is possible that the ion transport is more efficient in the extensive 2D pathways parallel to the planar electrodes in our system.

For BTTT/dEO4 and 4T/dEO4 films, the Li-salts are mainly incorporated into their disordered EO4 layers, whose structural arrangements are coupled to the ion transport

behavior. In the edge-on configuration, the (00L) diffraction intensity profile from WAXS can provide useful structural information on the relative thickness between the highly ordered electron-conducting layer and the less ordered EO4 layer as well as their interfacial roughness. To develop an interpretable model based on the (00L) intensity profile, MD simulations were performed on the BTTT/dEO4 system. In the well-separated layered structure, the layer thickness is largely determined by the intrinsic chemical structure of the molecule. To systematically alter the relative thickness, a series of BTTT/dEOn derivatives with different lengths of the EO segment was simulated and equilibrated (see Supporting Information S6.7.1). The relative thickness is ascertained by the number density profile of non-hydrogen atoms in the BTTT segment along the z-direction. For better comparison,

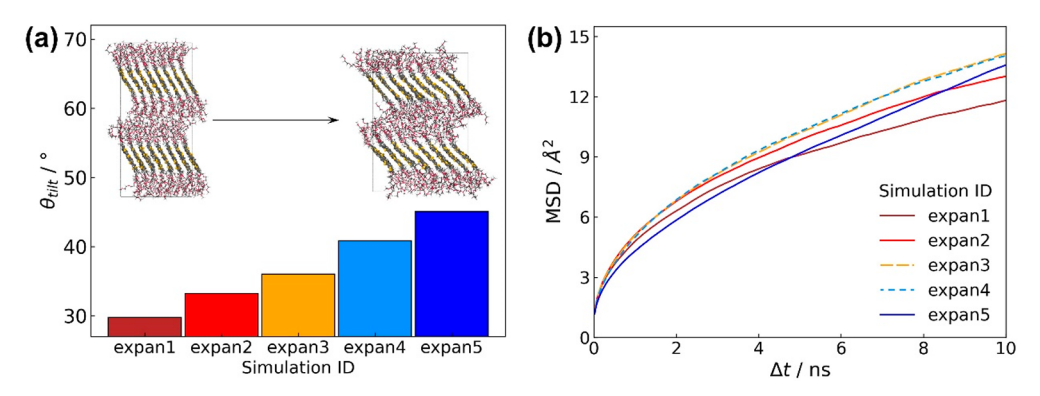


Figure 10. BTTT/dEO4 film expansion. (a) The average molecule tilt angle ($\theta_{\rm tilt}$) in BTTT/dEO4 configurations with different dimensions of the simulation box. Representative snapshots of selected simulations are shown as insets. (b) MSD plots of the EO4 segment in the simulated BTTT/dEO4 configurations with different box dimensions.

each density profile is plotted against the relative z position, which is obtained by scaling the original z position with its molecular layer thickness. The (00L) intensity profile of each BTTT/dEOn derivative is calculated accordingly, scaled by its maximum intensity. By extending the EO segment, the relative thickness of the ordered BTTT layer expectedly decreases, leading to the increase of the relative intensity for the (002) and (003) peaks (see Figure 9a,b). To change the interfacial roughness, different initial configurations were generated by shifting each BTTT/dEO4 molecule along its long-axis by a random amount and then equilibrated at 300 K (see Supporting Information S6.7.2). The interfacial roughness is also characterized by the density profile and the (00L) intensity profile is calculated by the same approach described above. As shown in Figure 9c,d, as the interfacial roughness increases, the relative intensities of the (002) and (003) peaks decrease until becoming barely detectable.

Rougher Interface at Low Temperature Improves Ionic Conductivity in BTTT/dEO4 Films. The (00L) profile was examined experimentally by T-WAXS of the neat BTTT/ dEO4 film. As the temperature increases, the (002) and (003) peaks become negligible above 20 °C, and the WAXS curves further become featureless above 80 °C (see Figure 9e), which is consistent with the transition from Sm1 to Sm2 to Iso phase identified by DSC. A similar phase behavior is expected when BTTT/dEO4 is mixed with the Li-salt, with the transition temperature shifted to lower values as confirmed by DSC (see Figure 3). For example, the melting temperature between the LC phase and the isotropic phase $(T_{\rm m})$ is shifted from 76.6 °C to 49.4 °C depending on salt concentration. According to thermal characterizations of 4T/dEO4, the material behaves more like a crystal so that the out-of-plane, long-range packing (presence of (001), (002), and (003) peaks) is maintained up to 106 °C. Doped with salt, the long-range packing of 4T/ dEO4 is preserved up to 96 °C as confirmed by temperaturedependent GIWAXS.24 For BTTT/dEO4 and 4T/dEO4, the relative thickness has minimal effect on the (00L) profile due to their similar chemical structure. All conductivity data were acquired from 30 to 100 °C in the experiment. When the temperature is below the melting point, the (00L) profiles indicate that the ion transport was probed in the layered structure of BTTT/dEO4 with rougher interfaces compared to 4T/dEO4. The interfacial roughness can reduce the π - π intermolecular interaction and alter the overall molecular behavior. To understand the trends of ion transport in the EO4 layer, MD simulations were performed to study the EO4segmental mobility in structures with different interfacial roughness as characterized in Figure 9c. The EO4-segmental mobility is estimated by the mean squared displacement (MSD) of oxygen atoms in the EO4 segment (see Figure 9f). The MSD plots show that a rougher interface gives rise to a more facile EO4-segmental motion and potentially a more efficient ion transport, 44,47-50 aligning with the conductivity difference between BTTT/dEO4 and 4T/dEO4 measured in the experiments below T_{m} . In hindsight, an increase in molecular packing disorder is a priori expected to enhance the mobility of any species residing therein, and higher interfacial roughness generates such an effect in the EO4 domain. Note that mobility improves with interfacial roughness only up to a point, as the molecular motion in the layered structure is restricted at a local scale. Further mobility improvement would require more drastic structural changes as brought about by a phase transition. When the temperature is above the $T_{\rm m}$, BTTT/dEO4 and 4T/dEO4 are anticipated to form analogous disordered phases due to their similar chemical structures, and thus have more comparable ionic conductivities.

Lateral Layer Expansion in BTTT/dEO4 at r = 0.1**Likely Promotes Ionic Conductivity.** As mentioned above, BTTT/dEO4 shows higher ionic conductivities than 4T/ dEO4 at all salt concentrations, and a significant conductivity difference is observed at r = 0.1. Apart from the rough interface formed at relatively low temperatures, other salt-induced structural rearrangements in BTTT/dEO4 may also play a role in facilitating ion transport. Overall, for r = 0.1 the structural order was largely suppressed in BTTT/dEO4, while it was enhanced in 4T/dEO4.41 Specifically, the in-plane film expansion was only detected in BTTT/dEO4 at different salt concentrations, which gave rise to the increase of the molecular tilt angle (see Figure 5). To simulate the film expansion, a series of initial configurations with the same density but different box dimensions was equilibrated at 300 K (see Supporting Information S6.7.3). The molecular tilt angle was calculated based on our previous definition (see Figure 10a). As the simulation box expands in the x-y plane, the BTTT segments tilt more toward the film plane, which tends to reduce the effective $\pi - \pi$ intermolecular interaction. The EO4segmental mobility estimated by computing its MSD (see Figure 10b) shows that the in-plane expansion promotes EO4segmental motion, thus potentially facilitating ion transport. Like the effect of interfacial roughness, the mobility promoted by the in-plane expansion is also bounded by local constraints imposed by the layered structure. The noticeable in-plane

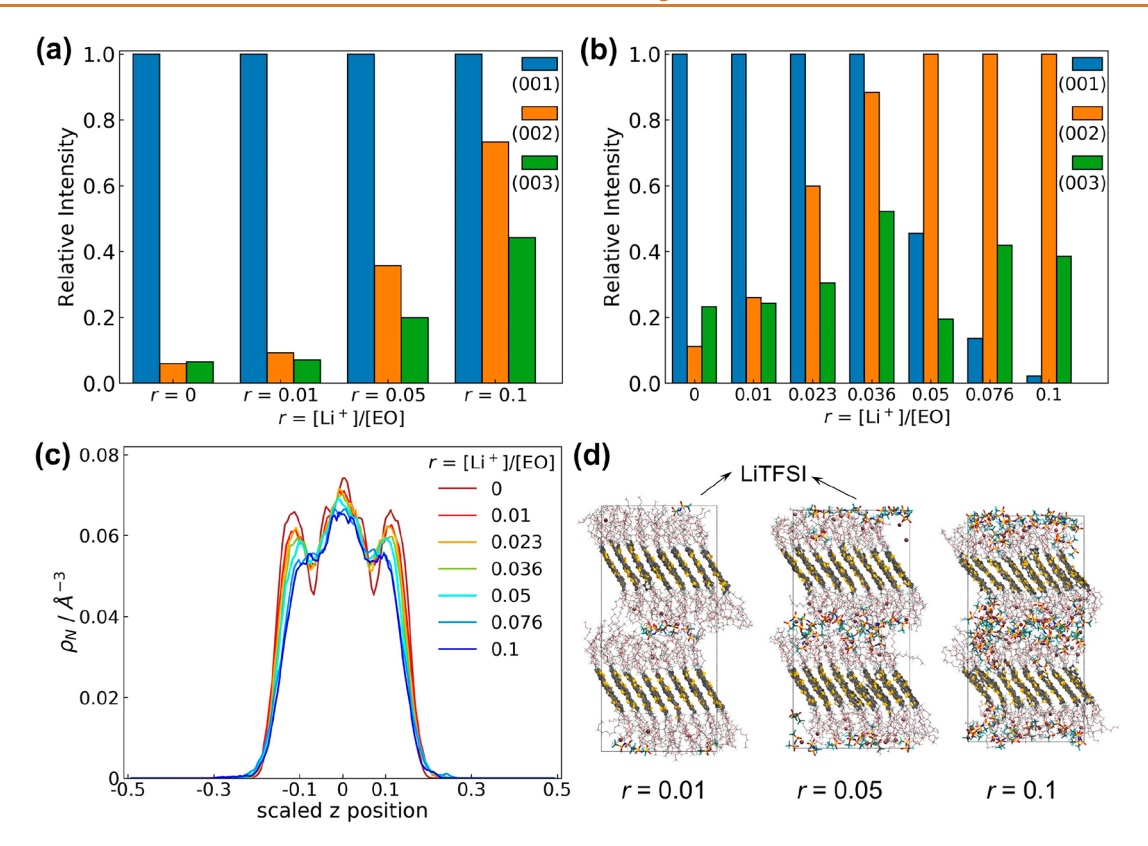


Figure 11. BTTT/dEO4 film mixed with Li-salt. (a) Integrated relative intensity profiles of the (00L) peaks for BTTT/dEO4 films at different salt concentrations obtained from experimental GIWAXS. (b) Relative intensity profiles of the (00L) peaks, and (c) number density profiles along the z-direction for simulated BTTT/dEO4 configurations at different salt concentrations. (d) Snapshots of simulated BTTT/dEO4 configurations at selected salt concentrations.

expansion of BTTT/dEO4 at r = 0.1, as observed experimentally, would then be a key contributor to its much superior ionic conductivity compared to 4T/dEO4.

Lastly, we briefly discuss the (00L) intensity profiles of BTTT/dEO4 at different salt concentrations, albeit this is less relevant to ionic conductivity. Based on the experimental GIWAXS of BTTT/dEO4 films, the (00L) intensity profiles at different salt concentrations are obtained from the vertical linecut analysis using GIXSGUL, 34 and each (00L) intensity profile is scaled by its maximum intensity. Figure 11a shows that the relative intensities of the (002) and (003) peaks increase significantly with salt concentration. Systems with different salt concentrations and proper film expansions were equilibrated at 300 K in MD simulations (see Supporting Information S6.7.4). In the simulated (00L) profiles, relative intensities of the (002) and (003) peaks also increase considerably with the salt concentration, and the (002) peak even shows the strongest intensity at higher concentrations (see Figure 11b). Based on our previous analysis, the relative thickness is examined using the density profile along the zdirection. However, the addition of Li-salt only slightly reduces the relative thickness of the BTTT layer (see Figure 11c), which plays a limited role in altering the (00L) profile. Our simulations further reveal that anions of the Li-salt tend to aggregate in the middle of the EO4 layer to form a region with relatively high electron density (see Figure 11d). These anion regions along with the ordered BTTT layers can create the destructive X-ray interference for the (001) scattering vector and the constructive interference for the (002) vector. This interference effect is stronger as the anion regions expand with

higher salt concentration, becoming the dominant contribution to the trend observed in the simulated (00L) profile. Note that the experimental and simulated (00L) profiles do not match quantitatively at similar salt concentrations, which is likely related to the complexity of the experimental BTTT/dEO4 film morphology. Our simulations focus on the layered structure of BTTT/dEO4, while the experimental BTTT/dEO4 films are usually composed of aggregation domains with layered structure and amorphous domains. The varying volume ratio of aggregation domains and the uneven salt distribution can generate extra interference in the experimental observations; for example, the local salt concentration in the layered structure could be lower than the average salt concentration in the whole film.

CONCLUSIONS

In this work, we synthesized BTTT/dEO4 LC and investigated its thermal behavior and structure with DSC, T-WAXS, GIWAXS, and POM. We found BTTT/dEO4 LC to self-assemble into a smectic layered structure with a spacing distance of 36.5 Å. We observed one exothermic and two endothermic events in the BTTT/dEO4 associated with the Sm1, Sm2, and isotropic phases. Considering the semicrystalline nature of BTTT/dEO4 films, we adopted an integrated approach of experimental GIWAXS and MD simulations to determine the molecular packing structure. MD simulations provided an important guide to interpret the experimental GIWAXS patterns, showing that the layer of BTTT segments was packed into the herringbone motif. For the BTTT/dEO4 films with different lithium salt concentrations, we calculated

several geometric parameters based only on the diffraction peak positions, revealing an anisotropic film expansion behavior. Additionally, we implemented crystallographic refinement to get an approximate estimation of the molecular orientation and alignment of the BTTT segment.

Ion conduction characteristics were assessed by blending BTTT/dEO4 with LiTFSI. The crystallinity in BTTT/dEO4 was slightly enhanced up to r=0.05 and suppressed at r=0.1. The melting temperature between the LC phase and the isotropic phase $(T_{\rm m})$ is shifted from 71.6 °C at r=0 to 49.4 °C at r=0.1. Ionic conductivities of BTTT/dEO4 were measured by EIS and found to be higher than those of 4T/dEO4 at all temperatures and salt concentrations. A complementary analysis of simulated models and experimental WAXS data indicates that ion conduction in BTTT/dEO4 is promoted by forming an irregular interface between the BTTT and EO4 layers at relatively low temperature and by the salt-induced lateral film expansion.

The results shown in this work demonstrate a valuable design principle for this class of LC. To enable high ionic conductivities in a LC, the formation of the smectic layered structure that is parallel to the interdigitated electrodes is a necessity, and a rougher layer interface leads to better ion conduction of the LC. The research interest in LC-based MIEC is rapidly increasing. Rationally designed LC materials with high dual conductivity can be potentially used for applications such as Li-ion batteries, 4,51,52 solar cells, 11 organic electrochemical transistors, 33 and water treatments. 4 However, the interplay between ionic and electronic transport mechanisms for MIEC materials is complicated. Further study is required to understand the electronic transport mechanism.

EXPERIMENTAL SECTION

Synthesis of BTTT/dEO4 and 4T/dEO4. All reagents and solvents were purchased from Sigma-Aldrich and AK Scientific and used as received unless otherwise noted. Anhydrous tetrahydrofuran (THF) was freshly distilled from calcium hydride prior to use. BTTT/dEO4 was synthesized via Suzuki coupling reaction. The synthesis route is shown in Figure S1. The structure of the final product was confirmed by ¹H and ¹³C NMR spectra (Figures S2 and S3). All the NMR experiments were conducted at room temperature on a Bruker AV-500 spectrometer. The detailed synthetic procedure and characterization of BTTT/dEO4 are provided in Supporting Information S1. The synthesis of 4T/dEO4 was described in our previous study.²⁴

Thermogravimetric Analysis. TGA was performed on a TA Instruments Discovery thermogravimetric analyzer at a heating rate of 20 °C/min. Samples were kept in a nitrogen environment. TGA results can be found in Supporting Information S2.

Differential Scanning Calorimetry. DSC measurements were performed on a TA Instruments Discovery 2500. A mixed solution of BTTT/dEO4 and LiTFSI at different *r* values was drop casted on DSC pans. Neat and salt blended BTTT/dEO4 samples were measured at scan rates of 5, 10, and 20 °C/min from -50 to 140 °C. Data from the first cooling scan and second heating scan were recorded for further analysis. Samples were kept under nitrogen flow during the measurements. DSC results can be found in Supporting Information S2.

Fabrication of Liquid Crystal Thin Films. An optimized film fabrication procedure, the "sit and cast" method, was developed to improve the film quality and obtain the uniform film thickness (see Supporting Information S3 for more details). The BTTT/dEO4 and 4T/dEO4 thin films with different lithium salt concentrations were prepared by this procedure. The produced thin films were then used for various experimental characterization methods, including polarized

optical microscopy, grazing-incidence wide-angle X-ray scattering, and electrochemical impedance spectroscopy.

Temperature-Dependent Wide-Angle X-ray Scattering. T-WAXS experiments were performed with SAXSLAB (XENOCS)'s GANESHA equipped with a T-95 Linkam stage at University of Chicago. LC material was dissolved in THF, and the solution was pipetted into a capillary. The solvent was then evaporated, and samples were measured in transmission mode of WAXS as a function of temperature.

Grazing-Incidence Wide-Angle X-ray Scattering, GIWAXS experiments were conducted at the Advanced Photon Source (Argonne National Laboratory) at beamline 8-ID-E. The energy of the incident beam was at 10.91 keV, and a Pilatus 1MF pixel array detector (pixel size = 172 mm) was used. GIWAXS images of thin films were taken at a grazing incident X-ray angle of 0.14°, which is above the critical angle of the sample film and below the critical angle of the silicon substrate. The measurement time for one image was 5 s. All samples were placed and measured in a low-vacuum chamber (10^{-3} mbar) to reduce the air scattering as well as to minimize beam radiation damage. There are multiple rows of inactive pixels between the detector modules when the images were collected at one position. To fill these inactive gaps, the detector was moved down to another preset position along the vertical direction after each measurement to collect image. The data from these two detector positions were combined using the GIXSGUI package³⁴ for MATLAB to fill the inactive gaps. The absence of artifacts in the combined image demonstrates that the scattering from the sample does not change during the exposure.

Polarized Optical Microscopy. An Olympus BX51 was used to monitor optical textures and thermal behaviors of BTTT/dEO4 and 4T/dEO4.

Atomic Force Microscopy. The LC film thicknesses were characterized by height images created from a Cypher ES AFM (Asylum Research Oxford) with an FS-15000AuD cantilever at room temperature. The LC material was deposited on top of a Si substrate with the "sit and cast" method. A clean cut was then made with a razor blade. The height images were acquired using tapping mode and analyzed using Gwyddion software. ⁵⁵

Electrochemical Impedance Spectroscopy. EIS measurements were performed on top of IDE arrays with a 1 μ m SiO₂ supporting layer using a Gamry 600+ potentiostat inside an argon-filled glovebox. The fabrication details can be found in our previous report. The EIS was then measured from 1 MHz to 0.1 Hz at different temperatures. The ionic resistance ($R_{\rm ion}$) data were then extracted from the impedance spectrum by fitting an equivalent circuit shown in the discussion section. The ionic conductivity σ_i of the thin film sample was calculated using the following equation:

$$\sigma_i = \frac{1}{R_{\text{ion}}} \times \frac{d}{l(N-1)h}$$

where $R_{\rm ion}$ = ionic resistance; d = spacing between adjacent electrode teeth, 8 μ m; l = length of the electrode, 1000 μ m; N = number of electrodes, 160; and h = thickness of the film.

Simulation Method. An all-atom model was used to generate thermally equilibrated configurations of BTTT/dEO4. Force field parameters are provided in Supporting Information S4. To generate the appropriate initial crystal configuration, several single-crystal structures of relevant chemical species were evaluated, and the $\alpha\textsc{-}4\textsc{T}/$ HT was eventually selected as the template. MD simulations based on the selected template were run at different temperatures and lithium salt concentrations to study the corresponding thin film structures. The simulated GIXD patterns were calculated under the kinematical framework using the equilibrated configuration obtained from the MD simulations. The orientation of the simulated configurations was set to be consistent with the experimental thin films as determined by the experimental GIWAXS patterns. Procedures of simulating the GIXD patterns are provided in the Supporting Information S5.

ACS Nano www.acsnano.org Article

ASSOCIATED CONTENT

Supporting Information

The Supporting Information is available free of charge at https://pubs.acs.org/doi/10.1021/acsnano.2c07789.

Synthesis of BTTT/dEO4 liquid crystal, thermal behaviors of BTTT/dEO4, processing and ionic conductivity measurements of liquid crystal thin films, computational modeling and MD simulation, GIXD simulation, observations and analysis method of GIXD simulation, and supplemental experimental GIXD data and related analysis result (PDF)

Force field parameters of all the chemical species simulated (ZIP)

AUTHOR INFORMATION

Corresponding Authors

Shrayesh N. Patel — Pritzker School of Molecular Engineering, University of Chicago, Chicago, Illinois 60637, United States; orcid.org/0000-0003-3657-827X; Email: shrayesh@uchicago.edu

Paul F. Nealey — Pritzker School of Molecular Engineering, University of Chicago, Chicago, Illinois 60637, United States; orcid.org/0000-0003-3889-142X;

Email: nealey@uchicago.edu

Christopher K. Ober — Department of Materials Science and Engineering, Cornell University, Ithaca, New York 14853, United States; orcid.org/0000-0002-3805-3314; Email: c.ober@cornell.edu

Fernando A. Escobedo — Smith School of Chemical and Biomolecular Engineering, Cornell University, Ithaca, New York 14853, United States; orcid.org/0000-0002-4722-9836; Email: fe13@cornell.edu

Authors

Zhongyang Wang — Pritzker School of Molecular Engineering, University of Chicago, Chicago, Illinois 60637, United States; Occid.org/0000-0002-3917-5268

Chaoqiuyu Wang — Department of Materials Science and Engineering, Cornell University, Ithaca, New York 14853, United States

Yangyang Sun — Smith School of Chemical and Biomolecular Engineering, Cornell University, Ithaca, New York 14853, United States; Occid.org/0000-0002-8499-5425

Kai Wang — Pritzker School of Molecular Engineering, University of Chicago, Chicago, Illinois 60637, United States Joseph W. Strzalka — X-ray Science Division, Argonne National Laboratory, Lemont, Illinois 60439, United States; orcid.org/0000-0003-4619-8932

Complete contact information is available at: https://pubs.acs.org/10.1021/acsnano.2c07789

Author Contributions

F.A.E., C.K.O., S.N.P., and P.F.N. conceived the project. Z.W. completed all sample preparations, performed DSC, TGA, T-WAXS, POM, GIWAXS, AFM, and EIS, and analyzed and oversaw all experimental data. C.W. and C.K.O. synthesized BTTT/dEO4 and performed NMR. Y.S. and F.A.E. performed MD simulations. K.W. fabricated IDEs. J.S. helped with GIWAXS measurements. All authors participated in manuscript preparation and editing.

Author Contributions

Z.W., C.W., and Y.S. contributed equally to this work.

Notes

The authors declare no competing financial interest.

ACKNOWLEDGMENTS

This work was supported by NSF DMREF Award Number 1922259. This research used resources of the Advanced Photon Source, an Office of Science User Facility operated for the U.S. Department of Energy (DOE) by Argonne National Laboratory under Contract No. DE-AC02-06CH11357. This work made use of the Pritzker Nanofabrication Facility part of the Pritzker School of Molecular Engineering at the University of Chicago, which receives support from Soft and Hybrid Nanotechnology Experimental (SHyNE) Resource (NSF ECCS-2025633), a node of the National Science Foundation's National Nanotechnology Coordinated Infrastructure. Parts of this work were carried out at the Soft Matter Characterization Facility of the University of Chicago. This work made use of the shared facilities at the University of Chicago Materials Research Science and Engineering Center, supported by National Science Foundation under award number DMR-2011854. This work made use of the Cornell Center for Materials Research Shared Facilities, which are supported through the NSF MRSEC program (DMR-1719875). This work used the Extreme Science and Engineering Discovery Environment (XSEDE), which is supported by the National Science Foundation grant number ACI-1053575.

REFERENCES

- (1) Tschierske, C. Microsegregation: From Basic Concepts to Complexity in Liquid Crystal Self-Assembly. *Isr. J. Chem.* **2012**, *52*, 935–959.
- (2) Kloos, J.; Joosten, N.; Schenning, A.; Nijmeijer, K. Self-assembling liquid crystals as building blocks to design nanoporous membranes suitable for molecular separations. *J. Membr. Sci.* **2021**, 620, 118849.
- (3) Bisoyi, H. K.; Kumar, S. Liquid-crystal nanoscience: an emerging avenue of soft self-assembly. *Chem. Soc. Rev.* **2011**, *40*, 306–319.
- (4) Sakuda, J.; Hosono, E.; Yoshio, M.; Ichikawa, T.; Matsumoto, T.; Ohno, H.; Zhou, H.; Kato, T. Liquid-Crystalline Electrolytes for Lithium-Ion Batteries: Ordered Assemblies of a Mesogen-Containing Carbonate and a Lithium Salt. *Adv. Funct. Mater.* **2015**, *25*, 1206–1212
- (5) Kuwabara, A.; Enomoto, M.; Hosono, E.; Hamaguchi, K.; Onuma, T.; Kajiyama, S.; Kato, T. Nanostructured liquid-crystalline Li-ion conductors with high oxidation resistance: molecular design strategy towards safe and high-voltage-operation Li-ion batteries. *Chem. Sci.* 2020, 11, 10631–10637.
- (6) Ichikawa, T.; Kato, T.; Ohno, H. 3D Continuous Water Nanosheet as a Gyroid Minimal Surface Formed by Bicontinuous Cubic Liquid-Crystalline Zwitterions. *J. Am. Chem. Soc.* **2012**, *134*, 11354–11357.
- (7) Ueda, S.; Kagimoto, J.; Ichikawa, T.; Kato, T.; Ohno, H. Anisotropic Proton-Conductive Materials Formed by the Self-Organization of Phosphonium-Type Zwitterions. *Adv. Mater.* **2011**, 23, 3071–3074.
- (8) Champagne, P.-L.; Ester, D.; Polan, D.; Williams, V. E.; Thangadurai, V.; Ling, C.-C. Amphiphilic Cyclodextrin-Based Liquid Crystals for Proton Conduction. *J. Am. Chem. Soc.* **2019**, *141*, 9217–9224.
- (9) Iino, H.; Usui, T.; Hanna, J.-i. Liquid crystals for organic thinfilm transistors. *Nat. Commun.* **2015**, *6*, 6828.
- (10) Shimizu, Y.; Oikawa, K.; Nakayama, K.-i.; Guillon, D. Mesophase semiconductors in field effect transistors. *J. Mater. Chem.* **2007**, *17*, 4223–4229.
- (11) Högberg, D.; Soberats, B.; Uchida, S.; Yoshio, M.; Kloo, L.; Segawa, H.; Kato, T. Nanostructured Two-Component Liquid-

- Crystalline Electrolytes for High-Temperature Dye-Sensitized Solar Cells. Chem. Mater. 2014, 26, 6496–6502.
- (12) Högberg, D.; Soberats, B.; Yatagai, R.; Uchida, S.; Yoshio, M.; Kloo, L.; Segawa, H.; Kato, T. Liquid-Crystalline Dye-Sensitized Solar Cells: Design of Two-Dimensional Molecular Assemblies for Efficient Ion Transport and Thermal Stability. *Chem. Mater.* **2016**, 28, 6493–6500.
- (13) Ni, J.-S.; Zhang, P.; Jiang, T.; Chen, Y.; Su, H.; Wang, D.; Yu, Z.-Q.; Kwok, R. T. K.; Zhao, Z.; Lam, J. W. Y.; Tang, B. Z. Red/NIR-Emissive Benzo[d]imidazole-Cored AIEgens: Facile Molecular Design for Wavelength Extending and In Vivo Tumor Metabolic Imaging. Adv. Mater. 2018, 30, 1805220.
- (14) Sakuda, J.; Yoshio, M.; Ichikawa, T.; Ohno, H.; Kato, T. 2D assemblies of ionic liquid crystals based on imidazolium moieties: formation of ion-conductive layers. *New J. Chem.* **2015**, *39*, 4471–4477
- (15) Xue, Z.; He, D.; Xie, X. Poly(ethylene oxide)-based electrolytes for lithium-ion batteries. *J. Mater. Chem. A* **2015**, *3*, 19218–19253.
- (16) Yuan, F.; Chi, S.; Dong, S.; Zou, X.; Lv, S.; Bao, L.; Wang, J. Ionic liquid crystal with fast ion-conductive tunnels for potential application in solvent-free Li-ion batteries. *Electrochim. Acta* **2019**, 294, 249–259.
- (17) Pingel, P.; Neher, D. Comprehensive picture of *p*-type doping of P3HT with the molecular acceptor F₄TCNQ. *Phys. Rev. B* **2013**, 87, 115209.
- (18) Iino, H.; Hanna, J.-i. Liquid crystalline organic semiconductors for organic transistor applications. *Polym. J.* **2017**, *49*, 23–30.
- (19) Tang, W.; Singh, S. P.; Ong, K. H.; Chen, Z.-K. Synthesis of thieno[3,2-b]thiophene derived conjugated oligomers for field-effect transistors applications. *J. Mater. Chem.* **2010**, 20, 1497–1505.
- (20) Dong, B. X.; Nowak, C.; Onorato, J. W.; Strzalka, J.; Escobedo, F. A.; Luscombe, C. K.; Nealey, P. F.; Patel, S. N. Influence of Side-Chain Chemistry on Structure and Ionic Conduction Characteristics of Polythiophene Derivatives: A Computational and Experimental Study. Chem. Mater. 2019, 31, 1418–1429.
- (21) Flagg, L. Q.; Bischak, C. G.; Onorato, J. W.; Rashid, R. B.; Luscombe, C. K.; Ginger, D. S. Polymer Crystallinity Controls Water Uptake in Glycol Side-Chain Polymer Organic Electrochemical Transistors. *J. Am. Chem. Soc.* **2019**, *141*, 4345–4354.
- (22) Conejo-Rodríguez, V.; Cuerva, C.; Schmidt, R.; Bardají, M.; Espinet, P. Li+ and K+ ionic conductivity in ionic nematic liquid crystals based on 18-diaza-crown ether substituted with six decylalkoxy-p-cyanobiphenyl chains. *J. Mater. Chem. C* **2019**, *7*, 663–672.
- (23) Feroci, M.; Civitarese, T.; Pandolfi, F.; Petrucci, R.; Rocco, D.; Zollo, G.; Mattiello, L. A series of new conjugated oligothiophenes for organic electronics. *AIP Conf. Proc.* **2020**, 2257, 020008.
- (24) Liu, Z.; Dong, B. X.; Misra, M.; Sun, Y.; Strzalka, J.; Patel, S. N.; Escobedo, F. A.; Nealey, P. F.; Ober, C. K. Self-Assembly Behavior of an Oligothiophene-Based Conjugated Liquid Crystal and Its Implication for Ionic Conductivity Characteristics. *Adv. Funct. Mater.* **2019**, 29, 1805220.
- (25) DiCésare, N.; Belletête, M.; Donat-Bouillud, A.; Leclerc, M.; Durocher, G. Substitutional Effects on the Structural, Spectroscopic, and Photophysical Properties of Quaterthiophenes and Sexithiophenes as Well as on Their Corresponding Polyesters. *Macromolecules* 1998, 31, 6289–6296.
- (26) Fichou, D. Structural order in conjugated oligothiophenes and its implications on opto-electronic devices. *J. Mater. Chem.* **2000**, *10*, 571–588.
- (27) Wu, W.; Liu, Y.; Zhu, D. π-Conjugated molecules with fused rings for organic field-effect transistors: design, synthesis and applications. *Chem. Soc. Rev.* **2010**, *39*, 1489–1502.
- (28) Cinar, M. E.; Ozturk, T. Thienothiophenes, Dithienothiophenes, and Thienoacenes: Syntheses, Oligomers, Polymers, and Properties. *Chem. Rev.* **2015**, *115*, 3036–3140.
- (29) Drzewicz, A.; Juszyńska-Gałązka, E.; Zając, W.; Piwowarczyk, M.; Drzewiński, W. Non-isothermal and isothermal cold crystallization of glass-forming chiral smectic liquid crystal (S)-4'-(1-

- methyloctyloxycarbonyl) biphenyl-4-yl 4-[7-(2,2,3,3,4,4,4-heptafluorobutoxy) heptyl-1-oxy]-benzoate. *J. Mol. Liq.* **2020**, *319*, 114153.
- (30) Yeates, S. G.; Teo, H. H.; Mobbs, R. H.; Booth, C. Ethylene glycol oligomers. *Die Makromol. Chemie* 1984, 185, 1559–1563.
- (31) Siegrist, T.; Kloc, C.; Laudise, R. A.; Katz, H. E.; Haddon, R. C. Crystal Growth, Structure, and Electronic Band Structure of α -4T Polymorphs. *Adv. Mater.* **1998**, *10*, 379–382.
- (32) Yuan, Q.; Mannsfeld, S. C. B.; Tang, M. L.; Toney, M. F.; Lüning, J.; Bao, Z. Thin Film Structure of Tetraceno[2,3-b]thiophene Characterized by Grazing Incidence X-ray Scattering and Near-Edge X-ray Absorption Fine Structure Analysis. *J. Am. Chem. Soc.* **2008**, 130, 3502–3508.
- (33) Yuan, Q.; Mannsfeld, S. C. B.; Tang, M. L.; Roberts, M.; Toney, M. F.; DeLongchamp, D. M.; Bao, Z. Microstructure of Oligofluorene Asymmetric Derivatives in Organic Thin Film Transistors. *Chem. Mater.* **2008**, *20*, 2763–2772.
- (34) Jiang, Z. GIXSGUI: a MATLAB toolbox for grazing-incidence X-ray scattering data visualization and reduction, and indexing of buried three-dimensional periodic nanostructured films. *J. Appl. Crystallogr.* **2015**, *48*, 917–926.
- (35) Mannsfeld, S. C. B.; Tang, M. L.; Bao, Z. Thin Film Structure of Triisopropylsilylethynyl-Functionalized Pentacene and Tetraceno-[2,3-b]thiophene from Grazing Incidence X-Ray Diffraction. *Adv. Mater.* **2011**, 23, 127–131.
- (36) Kirkpatrick, S.; Gelatt, C. D.; Vecchi, M. P. Optimization by Simulated Annealing. *Science* **1983**, 220, 671–680.
- (37) Hukushima, K.; Nemoto, K. Exchange Monte Carlo Method and Application to Spin Glass Simulations. *J. Phys. Soc. Jpn.* **1996**, *65*, 1604–1608.
- (38) Sharon, D.; Bennington, P.; Liu, C.; Kambe, Y.; Dong, B. X.; Burnett, V. F.; Dolejsi, M.; Grocke, G.; Patel, S. N.; Nealey, P. F. Interrogation of Electrochemical Properties of Polymer Electrolyte Thin Films with Interdigitated Electrodes. *J. Electrochem. Soc.* **2018**, *165*, H1028–H1039.
- (39) Sharon, D.; Bennington, P.; Dolejsi, M.; Webb, M. A.; Dong, B. X.; de Pablo, J. J.; Nealey, P. F.; Patel, S. N. Intrinsic Ion Transport Properties of Block Copolymer Electrolytes. *ACS Nano* **2020**, *14*, 8902–8914.
- (40) Onorato, J. W.; Wang, Z.; Sun, Y.; Nowak, C.; Flagg, L. Q.; Li, R.; Dong, B. X.; Richter, L. J.; Escobedo, F. A.; Nealey, P. F.; Patel, S. N.; Luscombe, C. K. Side chain engineering control of mixed conduction in oligoethylene glycol-substituted polythiophenes. *J. Mater. Chem. A* **2021**, *9*, 21410–21423.
- (41) Dong, B. X.; Liu, Z.; Misra, M.; Strzalka, J.; Niklas, J.; Poluektov, O. G.; Escobedo, F. A.; Ober, C. K.; Nealey, P. F.; Patel, S. N. Structure Control of a π -Conjugated Oligothiophene-Based Liquid Crystal for Enhanced Mixed Ion/Electron Transport Characteristics. *ACS Nano* **2019**, *13*, 7665–7675.
- (42) McMorrow, D.; Als-Nielsen, J. Elements of Modern X-ray Physics, 2nd ed., Wiley: West Sussex (U.K.), 2011.
- (43) Teran, A. A.; Mullin, S. A.; Hallinan Jr, D. T.; Balsara, N. P. Discontinuous changes in ionic conductivity of a block copolymer electrolyte through an order-disorder transition. *ACS Macro Lett.* **2012**, *1*, 305–309.
- (44) Zheng, Q.; Pesko, D. M.; Savoie, B. M.; Timachova, K.; Hasan, A. L.; Smith, M. C.; Miller, T. F., III; Coates, G. W.; Balsara, N. P. Optimizing ion transport in polyether-based electrolytes for lithium batteries. *Macromolecules* **2018**, *51*, 2847–2858.
- (45) Aziz, S. B.; Woo, T. J.; Kadir, M. F. Z.; Ahmed, H. M. A conceptual review on polymer electrolytes and ion transport models. *J. Sci: Adv. Mater. Devices* **2018**, *3*, 1–17.
- (46) Soberats, B.; Yoshio, M.; Ichikawa, T.; Ohno, H.; Kato, T. Zwitterionic liquid crystals as 1D and 3D lithium ion transport media. *J. Mater. Chem. A* **2015**, *3*, 11232–11238.
- (47) Zhu, W.; Yang, B.; Wang, X.; Wang, L.; Tang, X.; Yang, C. Structure and ionic conductive properties of polydioxolane-polyurethane-based electrolytes. *J. Appl. Polym. Sci.* **2002**, *83*, 103–111.
- (48) Kerr, R. L.; Edwards, J. P.; Jones, S. C.; Elliott, B. J.; Gin, D. L. Effect of varying the composition and nanostructure of organic

- carbonate-containing lyotropic liquid crystal polymer electrolytes on their ionic conductivity. *Polym. J.* **2016**, *48*, *6*35–*6*43.
- (49) He, R.; Kyu, T. Effect of Plasticization on Ionic Conductivity Enhancement in Relation to Glass Transition Temperature of Crosslinked Polymer Electrolyte Membranes. *Macromolecules* **2016**, 49, 5637–5648.
- (50) Johansson, A.; Gogoll, A.; Tegenfeldt, J. Diffusion and ionic conductivity in Li(CF3SO3)PEG10 and LiN(CF3SO2)2PEG10. *Polymer* **1996**, *37*, 1387–1393.
- (51) Javier, A. E.; Patel, S. N.; Hallinan Jr, D. T.; Srinivasan, V.; Balsara, N. P. Simultaneous electronic and ionic conduction in a block copolymer: application in lithium battery electrodes. *Angew. Chem., Int. Ed.* **2011**, *50*, 9848–9851.
- (52) Patel, S. N.; Javier, A. E.; Beers, K. M.; Pople, J. A.; Ho, V.; Segalman, R. A.; Balsara, N. P. Morphology and thermodynamic properties of a copolymer with an electronically conducting block: poly (3-ethylhexylthiophene)-block-poly (ethylene oxide). *Nano Lett.* **2012**, *12*, 4901–4906.
- (53) Kukhta, N. A.; Marks, A.; Luscombe, C. K. Molecular Design Strategies toward Improvement of Charge Injection and Ionic Conduction in Organic Mixed Ionic-Electronic Conductors for Organic Electrochemical Transistors. *Chem. Rev.* **2022**, *122*, 4325–4355.
- (54) Hamaguchi, K.; Ichikawa, R.; Kajiyama, S.; Torii, S.; Hayashi, Y.; Kumaki, J.; Katayama, H.; Kato, T. Gemini Thermotropic Smectic Liquid Crystals for Two-Dimensional Nanostructured Water-Treatment Membranes. ACS Appl. Mater. Interfaces 2021, 13, 20598–20605
- (55) Nečas, D.; Klapetek, P. Gwyddion: an open-source software for SPM data analysis. *Open Phys.* **2012**, *10*, 181–188.